



저작자표시-비영리-변경금지 2.0 대한민국

이용자는 아래의 조건을 따르는 경우에 한하여 자유롭게

- 이 저작물을 복제, 배포, 전송, 전시, 공연 및 방송할 수 있습니다.

다음과 같은 조건을 따라야 합니다:



저작자표시. 귀하는 원저작자를 표시하여야 합니다.



비영리. 귀하는 이 저작물을 영리 목적으로 이용할 수 없습니다.



변경금지. 귀하는 이 저작물을 개작, 변형 또는 가공할 수 없습니다.

- 귀하는, 이 저작물의 재이용이나 배포의 경우, 이 저작물에 적용된 이용허락조건을 명확하게 나타내어야 합니다.
- 저작권자로부터 별도의 허가를 받으면 이러한 조건들은 적용되지 않습니다.

저작권법에 따른 이용자의 권리는 위의 내용에 의하여 영향을 받지 않습니다.

이것은 [이용허락규약\(Legal Code\)](#)을 이해하기 쉽게 요약한 것입니다.

[Disclaimer](#)

Master of Science in Mechanical Engineering

Oil droplet impacting on the water  
surface: crater and jet dynamics  
depending on the oil viscosity

수면에 대한 기름 액적 충돌에 관한 연구:  
오일 점도에 따른 크레이터 및 제트 역학

August 2023

Graduate School of Mechanical Engineering  
Seoul National University

Hyunji Lee

Oil droplet impacting on the water  
surface: crater and jet dynamics  
depending on the oil viscosity

Advisor Hyungmin Park

Submitting a master's thesis of  
Mechanical Engineering

April 2023

Graduate School of Mechanical Engineering  
Seoul National University

Hyunji Lee

Confirming the master's thesis written by  
Hyunji Lee

June 2023

Chair	<u>Haecheon Choi</u>	(Signature)
Vice Chair	<u>Hyungmin Park</u>	(Signature)
Examiner	<u>Ho-Young Kim</u>	(Signature)

# Abstract

In this study, we conducted an experiment of the impacting of a silicon oil droplet (with varying viscosity) on a water in a deep-water tank at different impact velocities. The objective was to investigate the effects of the oil viscosity and Froude number on the dynamics of craters and jets formed on the surface of the water. By utilizing the high-speed shadowgraphy, we were able to measure the dimensions of the crater and multiple parameters of the jet. Through the analysis of the behavior of the jet, we categorized the subsequent phenomena into four regimes, and explained underlying mechanisms in terms of the viscosity variation and Froude number. The criteria for classifying the regimes are whether there is a pinch-off, whether the jet thickness is thinner than the initial droplet diameter, and whether the composition of the secondary droplet is oil only or mixed with water. In particular, two visualization methods were performed to check the composition of the secondary droplet. When we plotted the dimensionless crater width against the dimensionless time, we found that all the experimental cases were s-shaped curves that followed the same main curve and then separated, and the point of separation was determined by the Froude number. Additionally, particle image velocimetry (PIV) enabled us to acquire the velocity field surrounding the crater and conduct an energy analysis in terms of kinetic, potential, and surface energy, supporting the explained mechanism in each regime.

**Keyword** : droplet, crater, jet, pinch-off, secondary droplet, oil viscosity, energy conversion

**Student Number** : 2021-20098

# Table of Contents

Abstract .....	i
Table of Contents.....	iii
List of Tables .....	iv
List of Figures.....	v
Chapter 1. Introduction.....	1
Chapter 2. Experimental set-up and procedure .....	5
2.1. Oil droplet impact on water surface .....	5
2.2. Droplet generation and control of satellite droplets.....	7
2.3. High-speed two-phase particle image velocitmetry.....	8
2.4. Flow visualization .....	9
Chapter 3. Results and discussion .....	16
3.1. Regime classification.....	16
3.2. Energy analysis .....	21
3.3. Crater width.....	27
Chapter 4. Conclusion.....	44
Bibliography .....	47
Abstract in Korean.....	50

# List of Tables

Table 2.1. Summary of the parameter of the fluid considered in the present study.. .....	11
--	----

# List of Figures

Figure 2.1. Schematic diagram of oil droplet impact on the water surface experiment. Using the shadowgraphy technique, which involves placing a light source on the back of a test section to capture the shadows it creates .....12

Figure 2.2. Schematic diagram and various parameters of (a) crater; (b) jet .....13

Figure 2.3. (a) Schematic diagram of high-speed two-phase particle image velocimetry set up; (b) Raw image of the high-speed camera in (x- z) plane, when crater expands .....14

Figure 2.4. Schematic diagram of flow visualization by impact oil droplet (a) onto dyeing water; (b) onto water mixed with particle that only mixes with water .....15

Figure 3.1. Image of a 20cSt oil droplet impacting free surface at  $Fr=453$ , plotted over time with the moment of impact at  $t=0$ . The crater expands, reaches its maximum depth, contracts, and subsequently jets, and a pinch-off occurs from the rising jet, resulting in a secondary droplet.....29

Figure 3.2. Geometry of a jet for (a) Regime1(100cSt,  $Fr=211$ ), (b) Regime2(10cSt,  $Fr=113$ ), (c) Regime3(0.65cSt,  $Fr=604$ ), (d) Regime4(0.65cSt,  $Fr=680$ ).....30

Figure 3.3. Temporal variation of the height of jet for (a) Regime 1;

(b) Regime 2; (c) Regime 3; (d) Regime 4.  $t=0$  when a droplet impact the free surface.....31

Figure 3.4. Temporal variation of the height of jet for each regime plot on a single graph: Regime 1 (●), Regime 2 (●), Regime 3 (●), Regime 4 (●).....32

Figure 3.5. Temporal variation of the thickness of jet for each regime: Regime 2 (●), Regime 3 (●), Regime 4 (●).....33

Figure 3.6. The images of the jet when a 20 cSt oil droplet is dropped into the dyed water show that a secondary droplet of oil is formed.....34

Figure 3.7. The images of the jet that appears when (a) 10 cSt oil droplet; (b) 100cSt oil droplet is dropped into water mixed with water-only particles reveal the composition of the secondary droplet.....35

Figure 3.8. crater depth graph corresponding to (a) regime2; (b) regime3, 4.  $t=0$  is the moment of impact, and an image of the moment of retraction is shown below.....36

Figure 3.9. Regime map for Fr and Oh numbers: Regime 1 (●), Regime 2 (▲), Regime 3 (■), Regime 4 (★).....37

Figure 3.10. Illustration of the  $dV$  of the (a) crater and (b) jet to determine the potential energy .....38

Figure 3.11. Illustration of the  $A_{ow}$ ,  $A_{oa}$ , and  $A_{wa}$  of the (a) crater and (b) jet to determine the surface energy.....39

Figure 3.12. (a) Representation of the PIV results, where the 2-D results are three-dimensionalized through the axisymmetry assumption; (b) Illustration of the  $v_{jet}$  of the jet to determine the kinetic energy.....40

Figure 3.13. Surface energy, potential energy, kinetic energy, and gas-liquid interface position over time for (a) Regime 1, (b) Regime 2, (c) Regime 3, (d) Regime 4: surface energy( $\circ$ ), potential energy( $\Delta$ ), kinetic energy( $\times$ ), gas-liquid interface position( $-$ , orange line).....41

Figure 3.14. (a)  $t-w$  graph when 0.65cSt oil droplet impact, (b)  $\tau-w/D$  graph (Nondimensionalize).....42

Figure 3.15. Represent three cases for each viscosity,  $Fr=150-200$ ,  $350-400$ , and  $580-630$  (a) 0.65 cSt, (b) 50 cSt, and (c) 100 cSt. (d) Plotting the nine cases of (a), (b), and (c) on one graph to show that the points of departure from the curve are similar for each range of  $Fr$ . 0.65cSt( $\circ$ ), 50cSt( $\Delta$ ), 100cSt( $\square$ );  $Fr=150\sim 200$ ( $\bullet$ ),  $Fr=350\sim 400$ ( $\bullet$ ),  $Fr=580\sim 630$ ( $\bullet$ ) .....43

# Chapter 1

## Introduction

The study of drop impact on different surfaces is related to inkjet printing, rapid spray cooling of hot surfaces, and phenomena like aeration induced by raindrops striking the surface of rivers and oceans (Yarin, 2006). There have been many different studies on drop impact, including the shape of the droplet at impact (Chaudhuri *et al.*, 2022), whether the colliding surface is solid (Busmann *et al.*, 2006; Cossali *et al.*, 1997) or liquid, whether it is a deep pool (Deka *et al.*, 2017) or a liquid film, and whether the liquid and droplet are miscible or immiscible (Chen *et al.*, 2017; Yakhshi-Tafti *et al.*, 2010; Caviezel *et al.*, 2008). In the case of drop impact on a deep pool surface, Michon *et al.* (2017) found that experiments on various liquids led to the formation of a very high flow velocity accompanied by air entrainment beneath the water's surface.

In addition, Lee *et al.* (2020) investigated the air entrainment phenomenon that occurs when a droplet collides with a deep liquid pool, captured air evolution images using x-rays, and identified various forms of bubble breakup and pinch-off between the droplet and the liquid surface, as well as the conditions under which these phenomena occur. Comparing CFD and experimental results, Das *et al.* (2022) analyzed the dynamics of droplet collisions on a miscible surface. As a function of the number of Fr, they recorded the time for the jet to cut off and the ratio of the size of the secondary droplet to the diameter of the initial droplet. Dhuper *et al.* (2021) conducted experiments on immiscible conditions by colliding

kerosene droplets and water droplets on the surface of water, respectively, and discovered that depending on the Fr number, at  $Fr < 400$ , the radial expansion of the crater is followed by the contraction of the sidewall, and then the vertical contraction occurs, and at  $Fr > 400$ , where the impact velocity is high, the deeper and larger the crater becomes. According to the configuration of the jet, we also classified the regimes as no jet, short jet, singular jet, slender jet, and compound thick–thin jet. This investigation was conducted on a single type of droplet, and additional research is required to identify the water and kerosene components responsible for the observed results. In contrast, Lhuissier *et al.* (2013) analyzed the daughter droplets that occur down the crater in the oil bath when a water droplet is dropped into the oil bath and postulated two mechanisms dependent on the impact velocity that promote fragmentation by crater recession. There have been numerous studies on the collision of miscible and immiscible droplets in water basins, but it will be essential to investigate the collision of droplets in other liquids. Craters have also been examined in various ways, in addition to jets. Bisighini *et al.* (2010) presented an analytical model of the depth of a crater, presuming that the 2–D cross section of the crater is part of a circle, and compared and analyzed the model with experimental results from prior studies. In the experimental data comparison graph, it can be seen that the analytical model and the graph of the previous study are similar in the case of a large Fr, but in the case of a low Fr with a low impact velocity, the crater follows the theoretical model during expansion but deviates significantly from the analytical result during contraction. This is consistent with a previous study by

Dhuper *et al.* (2020), which demonstrated that when  $Fr$  is large, the crater contracts horizontally and vertically simultaneously, and the cross-section of the crater maintains the shape of a circle to some extent; however, when  $Fr$  is small, the sidewall contracts first and then contracts vertically, which is unsatisfactory, and the gap between the experimental results and the theoretical model is significant.

In addition, numerous numerical studies on the dynamics of drop impact have been conducted. There is a paper (Ma *et al.*, 2019) that numerically analyzes the drop impact phenomenon and energy conversion. Experiments were conducted to study the dynamics of the crater and the jet, and when the crater depth data was displayed simultaneously by taking a frontal and a side view, it was determined that the two graphs were nearly identical, allowing the analysis of the drop impact dynamics to be assumed to be axisymmetric. In addition, the energy conservation over time was demonstrated by numerical analysis, and at various  $We$  numbers, the surface energy and potential energy are maximized while the kinetic energy is minimized when the crater is at its maximum depth, and the reverse occurs when the jet occurs.

Numerous methods, such as experiments, CFD, and numerical calculations, have been used to examine the phenomenon of water droplets falling into deep water. However, when the droplet and the pool liquid are distinct, particularly if they are immiscible, the factors influencing the phenomenon are more complex and require a variety of experiments and analyses. Numerous parameters, including density, viscosity, and surface tension, have an effect on the phenomenon, and in-depth research is required to determine

how each parameter influences the phenomenon. When an oil droplet collides with the surface of water, we wish to examine how the droplet's viscosity influences the jet, crater, pinch-off, etc. Therefore, we would like to experiment with silicon oil by colliding it with deep water, which has a similar density to water and a similar surface tension for each viscosity, in order to observe the difference caused by the viscosity change. In addition to analyzing the shape of the crater, such as its depth and width, for the jet and crater dynamics, we will divide the regime of the jet, such as its height, thickness, and pinch-off, according to the Fr number and the viscosity of the droplet, and use energy analysis to determine the reason for the appearance of each regime.

## Chapter 2

### Experimental set-up and procedure

#### 2.1. Oil droplet impact on water surface

The experimental setup consists of a static acrylic water tank with dimensions of  $130 \times 130 \times 130 \text{ mm}^3$  along the transverse (x), longitudinal (y), and depth (z) directions, respectively [Figure 2.1]. The experimental vessel was filled to a height of 70mm with tap water at a temperature of 15 °C. To negate the effect of the wall effect when the droplet was released into water, the size of the water tank was set to be greater than 30 times the diameter of the target droplet (Dhuper *et al.*, 2021). To investigate the effect of viscosity on immiscible droplets, we deposited silicon oil droplets of varying viscosities and similar density to water onto the surface of the water. To observe the phenomenon that occurs when droplets collide by dropping them into the center of a deep pool of liquid, the needle was situated in the center of the tank and silicon oil was expelled by connecting the needle to a syringe pump (Fusion 100 Touch, Revodix Inc.). The droplet's impact velocity was determined by the droplet's drop location. To achieve this, the needle was mounted on a positioner that can be adjusted between 150 and 800 mm above the free surface. Using the equation  $v_{\text{impact}} = \sqrt{2gH}$ , the droplet has an adjustable impact velocity of 1.5 to 3.5 m/s where H is the height of needle from free surface. Silicon oil particles have viscosities of 0.65, 10, 20, 50, and 100 cSt. Except for the 0.65 cSt

case, silicone oil has a similar density to water as shown in Table 2.1. Additionally, while the surface tension of water and silicone oil are distinct, oil droplets of various viscosities have similar surface tension values, so the observed difference in behavior when dropped with the same impact velocity is not due to surface tension. The principal dimensionless numbers employed in this experiment are the Froude number ( $Fr = v_{impact}/\sqrt{gD}$ ,  $D$  : diameter of initial droplet) and the Ohnesorge number ( $Oh = \mu/\sqrt{\rho\sigma D}$ ).  $Fr$  and  $Oh$  varies by depending on the impact velocity and viscosity of the oil droplet.

As soon as the oil droplet strikes the surface of the water, a crater is formed in the water beneath the surface, and as the crater recedes after reaching its maximum depth, a stream is produced at its center, which is observed above the surface. Using shadowgraphy [Figure 2.1], a technique that captures the shadow cast by a backlight, the dynamics of the crater and jet were observed. On the opposite side of the light source, a computer-connected high-speed camera (RayPower 5000, Dantec Dynamics) was installed. Through a 100mm macro lens (Samyang), the high-speed camera acquired images at 4000–5000 fps. The unprocessed image is retained and subjected to binarization via image processing. The present study used the Matlab Sauvola method for image binarization. Various parameters are extracted from these images in order to analyze the dynamics of the crater and flow. For the crater, we measured the width ( $w$ ) of the crater near the surface and its depth ( $d$ ). To analyze the crater's energy, we also obtained the crater's volume, surface area, rate of depth change, etc. For an analysis of the jet's dynamics, we measured height ( $h_{jet}$ ) and

thickness ( $t_{\text{jet}}$ ) of jet, as well as its volume, surface area, and rate of ascent. In the analysis of the jet, particularly at the time when a secondary droplet is formed by pinching off the jet's tip, the secondary droplet is not recognized as a jet, but the portion excluding the secondary droplet is recognized and measured as a jet.

## 2.2. Droplet generation and control of satellite droplets

Connecting a needle to a syringe pump (Fusion 100 Touch, Revodix Inc.) to convey silicon oil at a flow rate of 0.05 ml/min. The diameter of the droplet is determined by the interior diameter of the needle and the liquid's surface tension. In a needle with an inner diameter of 2.27mm (12G), silicon oil with a surface tension of 20 mN/s produced a droplet with a diameter of 2.7mm. The diameter of the droplet was determined using the following equation (Dhuper et al., 2021).

$$D = (D_v D_h^2)^{1/3} \quad (1)$$

At the location where the oil droplet separates from the needle, a small satellite droplet is produced.

In this experiment, we constructed apparatus to observe the satellite droplet's collision with the primary droplet. The apparatus includes a sensor, a solenoid valve, an air cylinder with a flat plate, and a solenoid valve-connected compressor. When the initial droplet is expelled from the needle, the sensor located barely below

the needle detects it. After the sensor detects the principal droplet, a solenoid valve that closes after a predetermined amount of time is installed. A compressor is connected to one side of the solenoid valve, while an air cylinder with a flat plate is connected to the other side. When the primary droplet is detected, the flat plate moves horizontally to obstruct the satellite droplet. The air cylinder is installed beneath the needle and sensor, and the installation height and time for the solenoid valve to close after detecting a signal were determined through repetitive experimentation. This secondary droplet interception device was used to examine the crater and jet dynamics resulting from the collision of only primary droplet.

### 2.3. High-speed two-phase particle image velocimetry

High-speed two-phase particle image velocimetry was used to measure the liquid velocity field in the pool when a droplet is released into the deep pool and to observe the flow field around the crater (Maeng and Park, 2021; Kim and Park, 2022). Using a high-speed camera (SpeedSense M310, Dantec Dynamics), we execute high-speed two-phase PIV and obtain images of the liquid phase and crater (320 x 384 px resolution at 4000 fps) [Figure 2.3(a)]. For separating the crater region from the obtained image, we illuminate the rear of the tank with a red LED (675 nm wavelength) that can only penetrate the liquid phase. Consequently, the image depicts the crater region as a black body [Figure 2.3(b)]; this

technique is known as shadow image technique (SIT). The PIV seeding particles (PMMA Rhodamine-B, size ranging 1–20  $\mu\text{m}$ ) are illuminated by a green laser sheet (wavelength of 532 nm) created using a continuous-wave (CW) laser (RayPower 5000, Dantec Dynamics) in order to visualize the motion of the liquid phase.

For capturing the crater and particle images, a 100 mm macro lens (Samyang) and an orange filter (cut-off length 570 nm, Heliopan) are used to screen the green laser reflected from the crater. Consequently, the camera can only capture red light from the LED and fluorescent seeding particle. In addition, because the intensity of LED and fluorescent light differs, we are able to distinguish the particle from the LED background image. Cross-correlation using a rapid Fourier transform algorithm (interrogation window of 16 x 16 pixels and 75% overlap) is used to analyze images of seeding particles. Lee and Park, 2017, provide more information about the high-speed two-phase PIV.

## 2.4. Flow visualization

In the center of the crater, a jet is generated as it contracts. The configuration of the jet varies based on the initial droplet's impact velocity and viscosity. For all viscosities exceeding a certain impact velocity, the jet will deflect and a secondary droplet will form. The form differs according to the quantity of pinch-off locations. We utilized two visualization techniques to ascertain the composition of these secondary droplets.

The first one is to differentiate between water and oil by dyeing water. I filled the reservoir with colored water and impacted a drop

of transparent oil. As depicted in Figure 2.4(a), the water was sufficiently dyed to prevent light from traveling through, and the captured image of this experiment revealed that the water and oil could be distinguished.

The second visualization method employs particles. Fill a water bath with particles that dissolve only in water, and collide with oil droplet [Figure 2.4(b)]. A continuous-wave (CW) laser (RayPower 5000, Dantec Dynamics) was installed so that the laser sheet was located in the region where the droplets collide, a high-speed camera was installed so that the field of view was parallel to the laser sheet, and an LED (red, wavelength of 675 nm) was placed on the back of the tank so that the jet's dynamics could also be observed. To capture the jet, a high-speed camera equipped with a 100mm macro lens and concentrated on the water's surface captured images at 4000 fps. Based on the presence or absence of particles, we could determine the composition of the secondary droplet from these images. If the particles were visible, it was determined that the majority of them were water, and if they were scarcely visible, it was determined that the majority of them were oil.

	Kinematic Viscosity ( $\nu$ )	Viscosity ( $\mu$ )	Density ( $\rho$ )	Surface Tension ( $\sigma$ )
	[ $mm^2/s$ ]	[cP]	[ $kg/m^3$ ]	[mN/m]
15° C tap water	1.004	1.004	999.1	72.5
0.65cSt silicon oil	0.65	0.49399	759.98	15.9
10cSt silicon oil	10	9.349813	934.98	20.1
20cSt silicon oil	20	18.99962	949.98	20.6
50cSt silicon oil	50	47.99904	959.98	20.8
100cSt silicon oil	100	96.49807	964.98	20.9

Table 2.1. Summary of the parameter of the fluid considered in the present study.

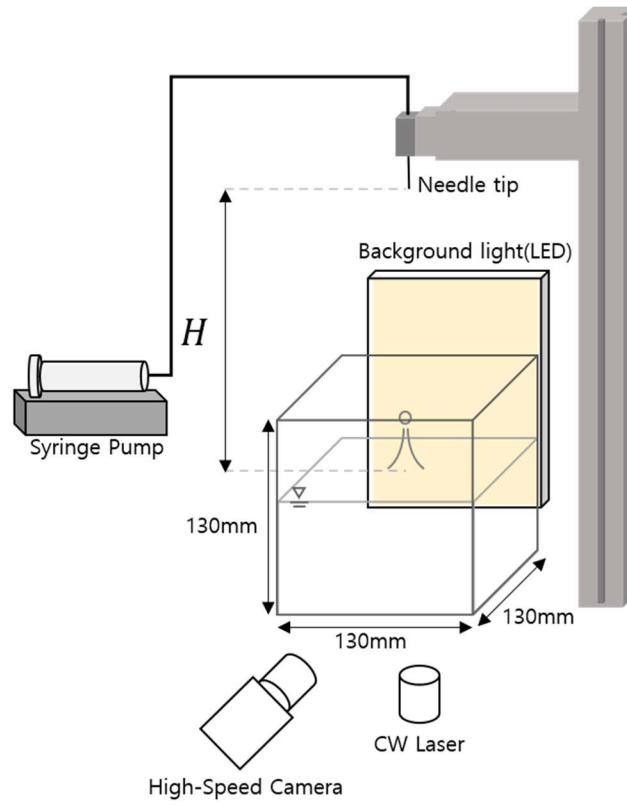


Figure 2.1. Schematic diagram of oil droplet impact on the water surface experiment. Using the shadowgraphy technique, which involves placing a light source on the back of a test section to capture the shadows it creates.

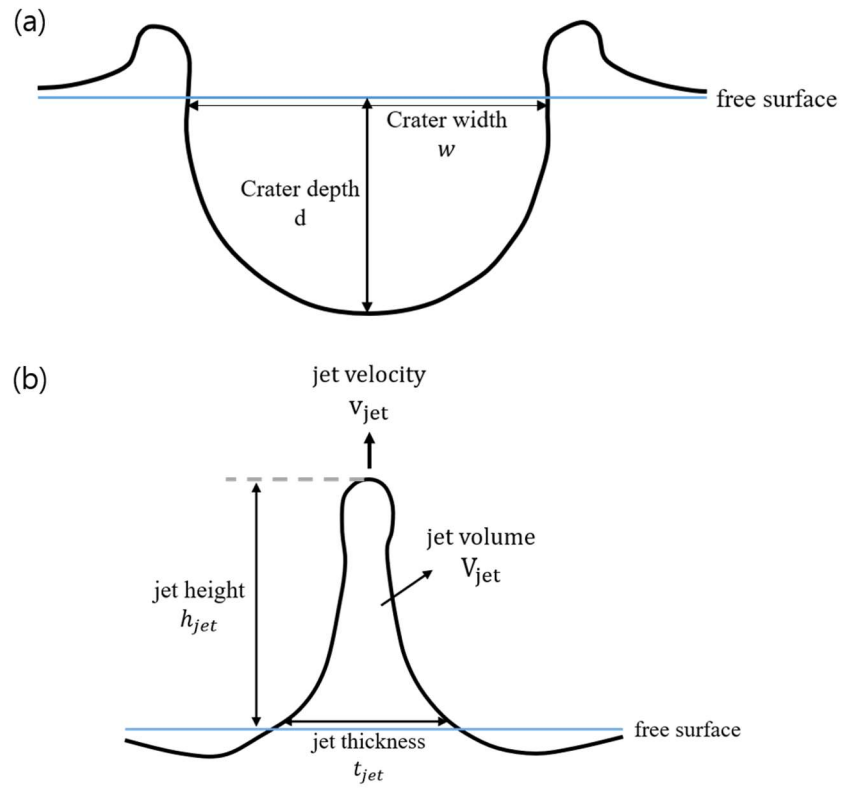


Figure 2.2. Schematic diagram and various parameters of (a) crater; (b) jet

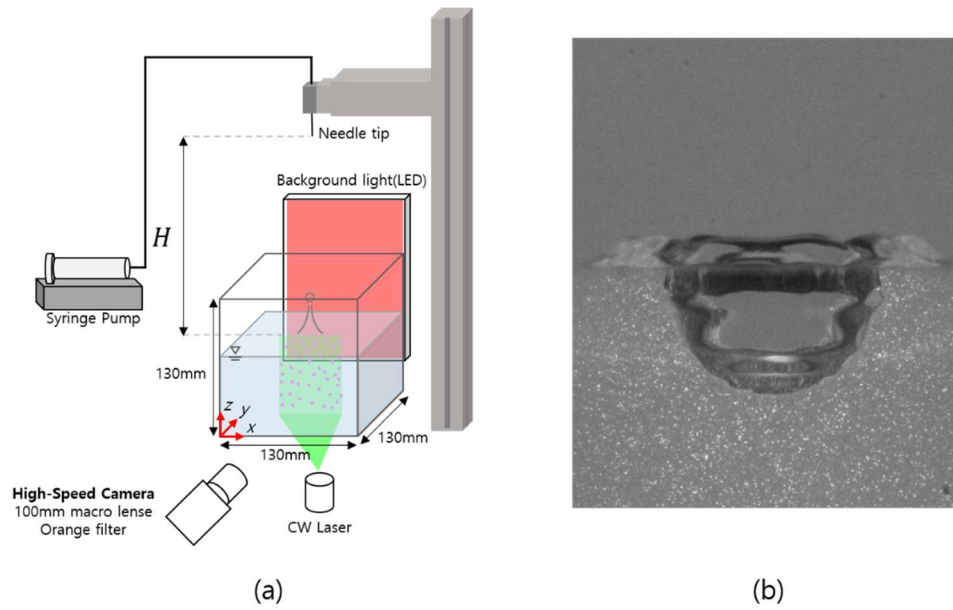


Figure 2.3. (a) Schematic diagram of high-speed two-phase particle image velocimetry set up; (b) Raw image of the high-speed camera in (x-z) plane, when crater expands.

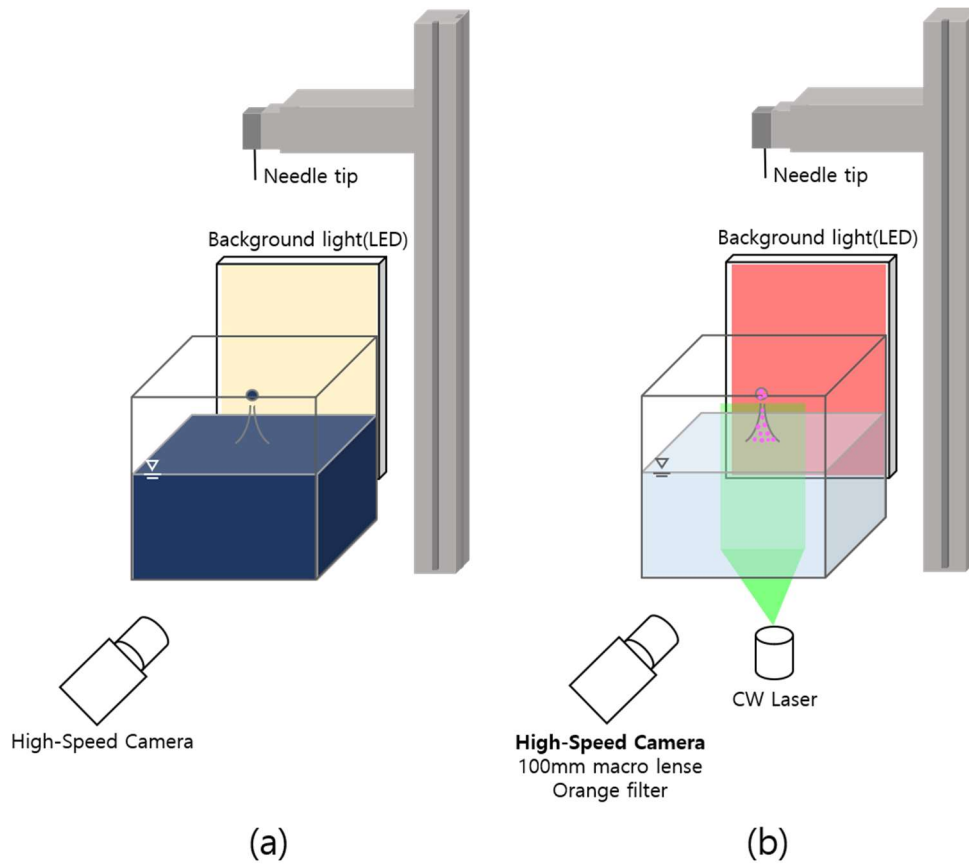


Figure 2.4. Schematic diagram of flow visualization by impact oil droplet (a) onto dyeing water; (b) onto water mixed with particle that only mixes with water

# Chapter 3

## Results and discussion

### 3.1. Regime classification

The instant the droplet strikes the free surface of the water tank, a crater is formed at the water's surface, which is indented by the impact, and a crown is formed along the crater's boundary above the surface of the water. The crater expands over time and recedes once it reaches its maximal depth and volume [Figure 3.1]. After the crater is retracted, a jet is observed above the free surface forming in its center. As the viscosity and Fr number of the droplet change, the time and location of the pinch-off also change, and different forms of jets have been observed. According to their characteristics, jet can be classified into four regimes.

- ✓ Regime 1: No pinch-off occurs
- ✓ Regime 2: Thin and fast jet formation
- ✓ Regime 3: Thicker jet with secondary droplet composition of oil
- ✓ Regime 4: Thicker jet, where the secondary droplet is a mixture of oil and water

Regime 1 is predominant at low Fr numbers and occurs when there is no pinch-off as the jet ascends. Since secondary droplets are not included in the jet, this is reflected in the jet height graph. Figure 3.3 is a plot of jet height ( $h_{jet}$ ) as a function of time, with 0 representing the instant when the jet begins to appear above the

surface of the water for each regime. In regime 1, where there is no pinch-off, the jet height is uninterrupted, whereas in regimes 2, 3, and 4, there are discontinuous dives. As time passes and the jet ascends, the jet height rises, and when the jet pinches off, the jet height graph abruptly decreases, resulting in a discontinuous graph. By examining these jump sections, the geometry of the pinch-off can also be determined. If you examine the jet height graph for each regime, you will notice that there is no abrupt break in regime 1. As the jet ascends in regime 2, we observe very small dives with pinch-offs, followed by severe dives with pinch-offs near the free surface. In the midst of the jet in regimes 3 and 4, we observe one or more pinch-offs with large secondary droplets. Comparing the graphs of regimes 3 and 4, you can see that both regimes have a pinch-off with a large satellite droplet. However, in regime 4, the pinch-off occurs and there is only one secondary droplet, whereas in regime 3, there are multiple pinch-offs, and even if there is only one pinch-off, there is another pinch-off in the secondary droplet, so there are more than two secondary droplets. Also, when regimes 1, 2, 3, and 4 are depicted on a single graph, the rate at which the jet rises is greatest in regime 2 [Figure 3.4].

The distinction between regime 2 and regimens 3 and 4 is the jet's thickness. Regime 2 is characterized by the presence of extremely narrow jets, and the criterion is  $t_{\text{jet}}/D=1$ . If the thickness of the jet is less than the diameter of the initial particle, it is categorized as regime 2 among instances of pinch-off in the jet. Figure 3.5 depicts the dimensionless jet thickness for dimensionless time, and the red line represents  $t_{\text{jet}}/D=1$ . Cases with values less than this red line were classified as belonging to regime 2.

The distinction between regime 3 and 4 relies on the secondary droplet composition. If the secondary droplet of jet consists primarily of oil, it is classed as regime 3, while if it consists of both oil and water, it is classified as regime 4. To determine the composition of secondary droplets, we carried out the two experiments outlined in Chapter 2.4 involving visualization.

The first is to distinguish between water and oil by flooding a bath with colored water and oil droplets that collide. Figure 3.6 depicts a series of images of the jet produced when a 20 cSt oil droplet is deposited into dyed water. In this image, the boundary where the secondary droplet forms, i.e. where the pinch-off occurs, consists of the colored water below and the uncolored oil above. This demonstrates that the secondary droplet in this instance is predominantly oil, corresponding to regime 3. As the viscosity change of the water caused by the dyeing process effects the maximum height of the jet, etc., this method necessitates a comparison with the experiment on pure water without any coloring. Comparing the case of 0.65 cSt,  $Fr = 604$  in Figure 3.2(c) with the case of dyed water in Figure 3.6, it can be seen that in both images, a boundary due to the difference in refractive index between water and oil is observed and pinch-off occurs at this boundary, and the secondary droplets that are observed and pinch-off occurs at this boundary are composed primarily of oil. Figure 3.2(c) thus corresponds to Regime 3. Also, if you compare Figure 3.6 to Figure 3.2(d) for the 0.65 cSt,  $Fr = 680$  case, you can see that the boundary between oil and water is observed, but the pinch-off occurs further down, indicating that the secondary droplet is composed of both water and oil. Thus, the situation depicted in

figure 3.2(d) corresponds to regime 4.

The second method is particle-based visualization. By filling a water tank with particles that only mix with water, dropping oil droplets, and installing a laser sheet through the center of the jet, we were able to capture images of the particles contained in the jet and the secondary droplets of the jet using a high-speed camera. Since the particles are only mixed with water, if no particles are observed, they compose of only oil, whereas if particles are observed, they must contain water. In the Figure 3.7(a), few particles are observed above the pinch-off boundary, whereas there are numerous particles below the boundary. In other words, the secondary droplet resulting from the pinch-off corresponds to regime 3, which consists primarily of oil. In Figure 3.7(b), a large number of particles are observed in both the secondary droplet and the flow above it. This indicates that the secondary droplet is composed of a mixture of water and oil, which corresponds to regime 4. In addition, if the size of the secondary droplet is larger than the initial droplet, it corresponds to regime 4, as the secondary droplet consists of both oil and water.

The difference in crater depth between regime 2 and regimes 3, 4 can also be observed. Figure 3.8 depicts the crater depth of the cases corresponding to regimes 2, 3, and 4 as a function of time, with time equal to zero at the moment of impact. The difference in crater profundity between regime 2 and regimes 3, 4 can also be observed. Figure 3.8 depicts the crater depth of the cases corresponding to regimes 2, 3, and 4 as a function of time, with time equal to zero at the moment of impact. In every instance, the crater's depth increases as it becomes deeper and then decreases

once it reaches its maximum depth. Examining the crater's retraction section reveals that in regime 2 [Figure 3.8(a)], the retraction is abrupt just before the jet occurs, in contrast to regimes 3 and 4 [Figure 3.8(b)], in which the retraction is gradual. As the crater's retreat is abrupt, it can be supposed that the jet's ascent velocity is also swift.

When oil droplets were deposited into a deep water tank, we classified four regimes based on the jet pinch-off, thickness, and composition of secondary droplets. The experimental cases are represented by the Fr and Oh numbers on a regime map [Figure 3.9]. Regime 1 is represented by a red circle, Regime 2 by an orange triangle, Regime 3 by a green square, and Regime 4 by a blue star. Observing the map of regimes, you can see that each regime appears in clusters of regions. In regime 1, the initial droplet's kinetic energy is too low, or its energy is not well converted to the kinetic energy of the jet, so the jet cannot rise to pinch off and pinch off does not occur. On the regime map, regime 1 is predominantly represented by low Fr numbers and high viscosity. For 0.65-20 cSt, there was no indication of regime 1 in the low Fr range. Although we did not conduct experiments with Fr less than 100 in this study, we can speculate that regime 1 may also occur at low viscosities between 0.65 and 20 cSt, where the initial droplet has less energy, i.e. a lower Fr. Regime 2, characterized by a succession of thin, rapidly ascending, small secondary droplets, was observed at low viscosities between 0.65 and 20 cSt and low Fr numbers between 100 and 200. Regime 3, which produces primarily oil-based secondary droplets, occupied the largest area and was found in a broad range of viscosity values ranging from 200 to 700.

As the viscosity increased, Regime 4, in which the secondary droplets consisted of a mixture of oil and water, occurred primarily at high Fr numbers but also at lower Fr numbers. In the low viscosity range of 0.65 to 20 cSt, regime 2, characterized by a narrow jet at low Fr, appears, while regime 3 emerges as Fr increases. At high viscosity, regime 2 does not exist, and as Fr increases, the viscosity transitions from regime 1 to regime 3 to regime 4. At 100 cSt, regime 3 is completely absent and regime 1 is immediately replaced by regime 4. When Fr is between 100 and 200, the height of the jet is very low and there is no pinch-off at high viscosity, whereas at low viscosity, the jet reaches a very high height and multiple pinch-offs occur at the same Fr number. Even at the Fr number of 600-700, the viscosity of the oil droplet divided it into regime 3 and regime 4.

### 3.2. Energy analysis

As demonstrated in Chapter 3.1, the jet dynamics vary greatly depending on whether the oil droplet is low or high viscosity at the same Fr number, such as no pinch-off at high viscosity and very high and rapid jet formation when a low viscosity oil droplet is struck at  $Fr = 150$ . Through energy analysis, we will determine the reason for this difference. In this experiment, the primary energy components are gravitational potential energy, surface energy, kinetic energy, and viscous dissipation (Ma *et al.*, 2019). To obtain the volume, surface area, etc. from the high-speed camera image and derive these values from the 2-D image, it is necessary to

assume that all phenomena are axisymmetric in order to analyze the energy of phenomena that occur when a droplet collides with a liquid surface, such as craters and jets. This assumption of axisymmetry applies to the calculation of gravitational potential energy, surface energy, and kinetic energy.

For each crater and jet, total energy ( $E_{\text{tot}}$ ) the sum of gravitational potential energy ( $E_p$ ) surface energy ( $E_s$ ), and kinetic energy ( $E_k$ ). Using subscripts, the distinction between crater and jet becomes apparent. Potential energy ( $E_p$ ) of the crater is the amount of work required to raise the liquid cavity's contents to the liquid's original, undisturbed surface. As shown in Equation (2), gravitational potential energy was obtained.

$$E_p = \int \rho gh dV \quad (2)$$

Finding the volume corresponding to each depth, multiplying it by the depth, and integrating yielded the crater's  $E_{p,c}$ . The image captured by the high-speed camera was binarized using Matlab image processing to convert the unprocessed image into a binary array. The diameter of the part corresponding to each depth was derived from the binary image, and the volume was determined by assuming axial symmetry [Figure 3.10(a)]. The crater's potential energy was calculated by multiplying the volume by the depth, density, and gravitational acceleration, then integrating the result. When a droplet collides with the surface of a liquid, a crater forms below the free surface and a crown forms above. Likewise, the potential energy of the crown was calculated in the way described above.  $E_{p,j}$  for jets was calculated similarly to  $E_{p,c}$  by locating the volume corresponding to each height under the assumption that it is axisymmetric, multiplying the volume by the height, density, and

gravitational acceleration, and integrating [Figure 3.13(a)]. Potential energy is proportional to the energy of the initial droplet, but it increases as the crater expands from the moment of impact, reaches its maximum value when the crater reaches its maximum depth, and decreases as the crater recedes. As the jet occurs, the value increases marginally and decreases as it descends.

Surface energy ( $E_s$ ) is the energy that results from the surface tension between air and water, air and oil, and oil and air. Equation (3) represents the surface energy expression.

$$E_s = \sigma_{wa}(A_{wa} - A_0) + \sigma_{ow}A_{ow} + \sigma_{oa}A_{oa} \quad (3)$$

$\sigma_{wa}$ ,  $\sigma_{wo}$ , and  $\sigma_{oa}$  are, in order, the surface tension values between water and air, water and oil, and oil and air. The values of  $\sigma_{wa}$  and  $\sigma_{oa}$  are displayed in Table 2.1, while the values of  $\sigma_{wo}$  are calculated through experiments in the paper of. The corresponding values of 51mN/m are used because the phenomenon is covered within 0.01 seconds after the collision (Goebel & Lunkenheimer, 1997)  $A_{wa}$ ,  $A_{wo}$ , and  $A_{oa}$  are the surface areas between water and air, water and oil, and oil and air, respectively, and  $A_0$  is the original surface area before the impact. To calculate the crater's surface energy, we find  $A_{wo}$ , and  $A_{oa}$ .  $A_{wa}$  is zero because the calculation implies that the oil spreads throughout the crater. Due to the fact that the image captured by the high-speed camera can only depict the boundary between air and liquid,  $A_{oa}$  can be derived from the experiment's image. Nevertheless, since  $A_{wo}$  cannot be distinguished from the image captured by the camera, the assumption that the oil film spreads throughout the crater allows us to determine that there is a boundary between oil and water where the boundary between oil and air has moved while maintaining its shape. Therefore, we can

find the boundary between oil and water by moving the boundary between oil and air and letting the volume between them be the volume of the initial oil droplet [Figure 3.11(a)]. Since the volume of the oil droplet is very small in comparison to the volume of the crater, we assumed that the ratio of  $A_{wo}$  to  $A_{oa}$  would be close, and when we calculated it, we discovered that  $A_{wo}$  was approximately 1.02 times the value of  $A_{oa}$  as the crater grew. We used  $A_{ow}$  and  $A_{oa}$  to calculate the crater's surface energy. Assuming that the oil is on top of the jet, we can determine its surface area in order to calculate its surface energy. We determined the portion of the jet where oil exists by locating the boundary whose volume is equal to that of the initial oil droplet. According to the division, the surface area where the oil meets the air is  $A_{oa}$ , and since the remainder of the jet can be thought of as water, the area where the water meets the air is  $A_{wa}$ . We determined  $A_{wo}$  to be the area corresponding to the boundary between oil and water [Figure 3.11(b)]. By substituting the surface area into the surface energy Equation (3), the surface energy of the flow was calculated.

Finally, the kinetic energy was computed by dividing it into portions and determining the velocity and volume of each portion using Equation (4).

$$E_{k,PIV} = \int \frac{1}{2} \rho v^2 dV$$

$$E_{k,oil} = \frac{1}{2} \rho_{oil} V_{droplet} v_{crater}^2 \quad (4)$$

$$E_{k,jet} = \frac{1}{2} \rho V_{jet} v_{jet}^2$$

Since the kinetic energy of the liquid in the liquid pool changes considerably when the droplet collides with the liquid pool, we measured the velocity field of the liquid pool using the high-speed

2-phase PIV described in Chapter 2.3. The flow field of the liquid pool was measured by PIV, but because it is a 2-D PIV, the volume was obtained by dividing each point with velocity information and three-dimensionalizing each part based on the axisymmetry assumption, and the kinetic energy was obtained by adding the assumption that the velocity magnitude is constant within the volume [Figure 3.12(a)]. The kinetic energy of a crater was calculated by adding the kinetic energy of the oil droplet to the previously calculated kinetic energy of the liquid pool. The rate of change in depth of the crater with respect to time is the velocity of the oil droplet. The mass of the oil droplet is obtained by multiplying the volume of the oil droplet by the density of each silicon oil. The jet's kinetic energy was calculated by adding the jet's kinetic energy to the liquid pool's kinetic energy, which was determined using PIV. The jet's kinetic energy was determined by presuming that the entire volume of the jet is equal to its velocity and using the jet's rate of height change as its velocity [Figure 3.12(b)].

Viscous dissipation is comprised of the terms viscosity, the square of the velocity gradient,  $dt$ , and  $dx$ , where the square of the velocity gradient,  $dt$ , and  $dx$  are, respectively, 4,  $-3$ , and  $-3$  to the 10th power. At low viscosity, viscosity is on the order of  $-6$  to the power of 10 and energy is on the order of  $-8$  to the power of 10, which is negligible in comparison to kinetic energy. High viscosity, on the other hand, has an order of  $-4$  to the power of 10, so the order of energy is  $-6$  to the power of 10, making it a meaningful term. Figure 3.13 is a graph of energy and the position of the gas-liquid interface over time, with circles representing surface energy,

triangles representing potential energy, and x symbols representing kinetic energy. The position of the gas–liquid interface indicates the crater's depth and the jet's height, which is indicated by the orange line. The crater expands, reaches its maximal depth, retracts, and then jets after the collision. Figure 3.13(a) is displayed during the regime1 phase. During expansion, kinetic energy is transformed into potential energy and surface energy. Due to the high viscosity, very little energy is converted back to kinetic energy as the object retracts, indicating viscous dissipation. Consider now the regime2 case of low viscosity for the same Froude number [Figure 3.13(b)]. In this instance, an extremely high and slender jet is produced. During the process of expansion, we observe the same energy conversion as in the previous case. In contrast to the preceding case, when retracting there was sufficient conversion to kinetic energy, resulting in a high jet. Consider now regimens 3 and 4 with Fr number of 300 [Figure 3.13(c~d)]. In regime 3, a maximal height jet is followed by a sharp pinch–off. Because viscous dissipation is negligible at low viscosity, there is a great deal of energy conversion during expansion and then a great deal of conversion to kinetic energy, resulting in a high flow. Despite having the same Fr number, 10cSt has a maximum jet height of 20mm while Regime4 has a relatively modest jet height of 14mm. This is due to the decrease in kinetic energy caused by high viscosity–induced viscous dissipation. In consequence, a higher jet was unable to form, and an oil–water secondary droplet was produced.

### 3.3. Crater width

In addition to its depth, the breadth of the crater was analyzed to characterize its geometry. The diameter of a crater measured from the surface defines its breadth. As the crater expands and contracts, so does its breadth, which we've plotted over time. Figure 3.14(a) is a graph of a collision with a 0.65 cSt particle whose Fr number ranges from 150 to 600. The x-axis represents time ( $t$ ), where  $t = 0$ s is the instant the particle strikes the surface of the water and  $t$  is the time elapsed since impact. Image processing yields the breadth of the crater along the y-axis. Each color corresponds to one Fr carton. As indicated by the graph, crater width increases with increasing Fr values. In all cases,  $w$  exhibits an s-shaped increase with time after impact and a subsequent decrease.

Figure 3.14(b) shows that  $t$  on the x-axis and  $w$  on the y-axis are dimensionless as  $\tau = t \times v_{\text{impact}} \times \frac{1}{D}$  and  $w/D$ , respectively, when examining the trend of these width graphs. On the graph of crater width and dimensionless time, an s-curve appears, as depicted in Figure 3.14(b), but the main curve, which increases with time after impact, follows the same curve and has a distinct separation point in each case. The larger Fr number also has a separation point at a larger dimensionless time. We plotted  $\tau$ - $w/D$  at 0.65, 50, and 100 cSt to examine the impact of viscosity on the main curve and separation point. At each viscosity, three cases spanning the Fr number ranges of 150–200, 350–400, and 580–630 were plotted [Figure 3.15]. Each viscosity is represented by a symbol, with 0.65 cSt represented by a circle, 50 cSt represented by a triangle, and 100 cSt represented by a square. The Fr number is represented by

a color, with red for the cases with the lowest impact velocity (150–200), green for 350–400, and blue for the cases with the highest impact velocity (580–630). As shown in Figure 3.15(a~c), all three viscosities follow a single primary curve and break away from the main curve at the separation point, with a larger  $\tau$  for larger Fr. The three graphs were combined in order to visualize the difference between the main trajectory of the graph corresponding to each viscosity and the  $\tau$  at which the separation point occurs depending on Fr [Figure 3.15(d)]. The main curves of the nine curves converge to one, and the curves of the same color converge to one line. This indicates that the separation points away from the main curve are nearly identical between cases with the same Fr range. In other terms, Fr determines  $w/D$  for dimensionless time. Only the separation points distant from the main curve are determined by Fr, irrespective of the droplet's impacting surface viscosity. Consequently, the crater breadth is a parameter independent of the droplet's viscosity.

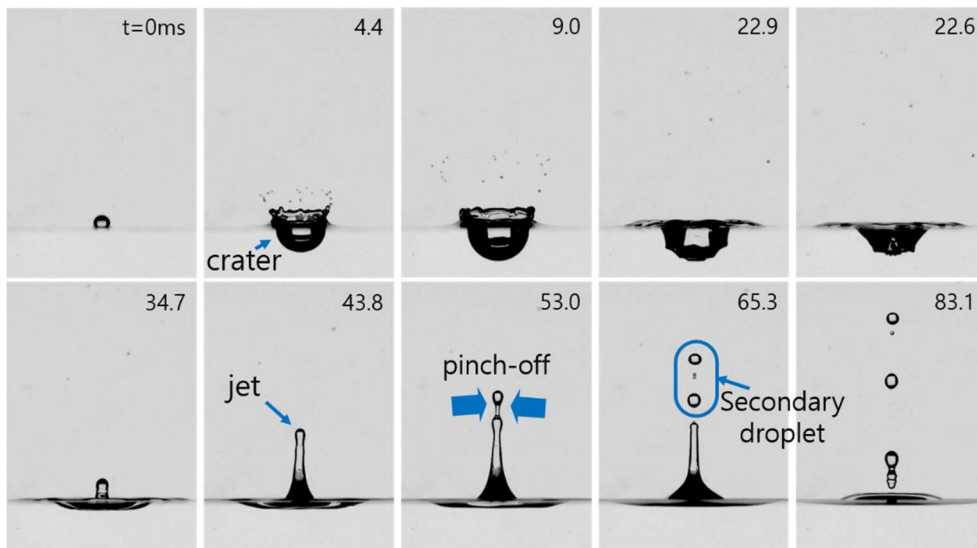


Figure 3.1. Image of a 20cSt oil droplet impacting free surface at  $Fr=453$ , plotted over time with the moment of impact at  $t=0$ . The crater expands, reaches its maximum depth, contracts, and subsequently jets, and a pinch-off occurs from the rising jet, resulting in a secondary droplet.

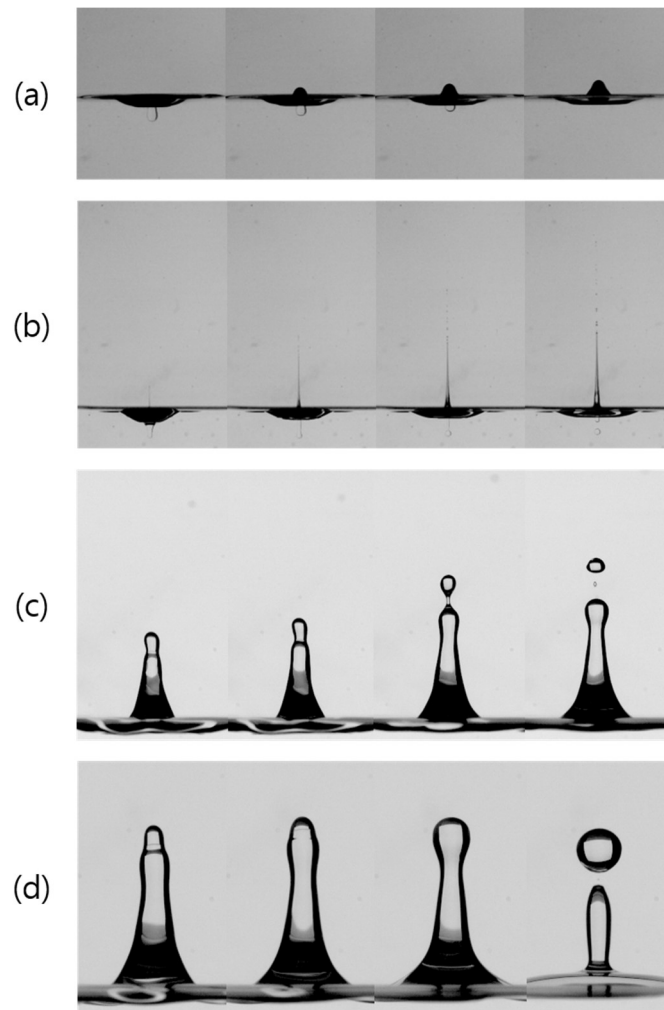


Figure 3.2. Geometry of a jet for (a) Regime1 (100cSt,  $Fr=211$ ), (b) Regime2 (10cSt,  $Fr=113$ ), (c) Regime3 (0.65cSt,  $Fr=604$ ), (d) Regime4 (0.65cSt,  $Fr=680$ ).

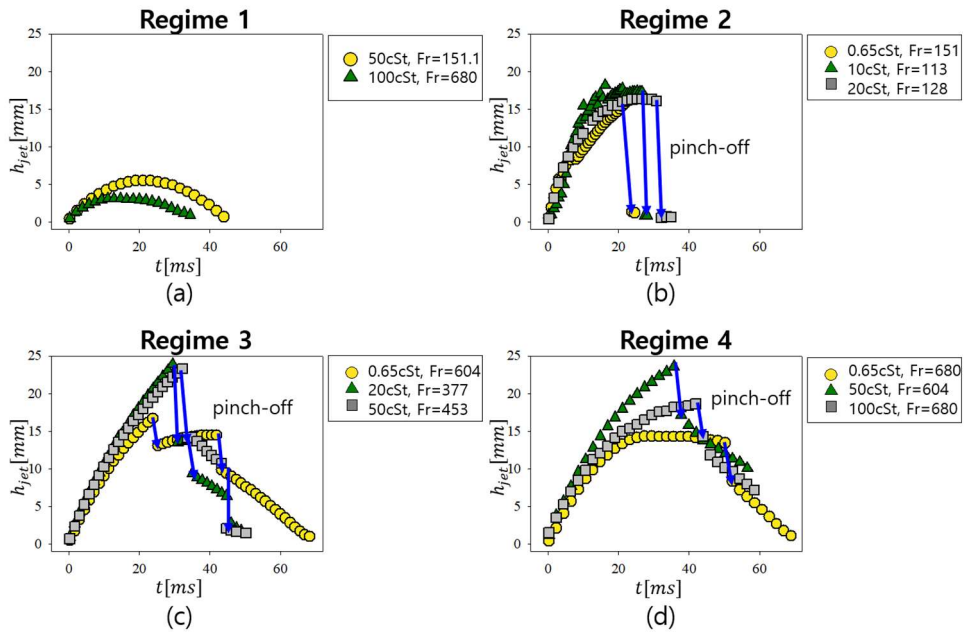


Figure 3.3. Temporal variation of the height of jet for (a) Regime 1; (b) Regime 2; (c) Regime 3; (d) Regime 4.  $t=0$  when a droplet impact the free surface.

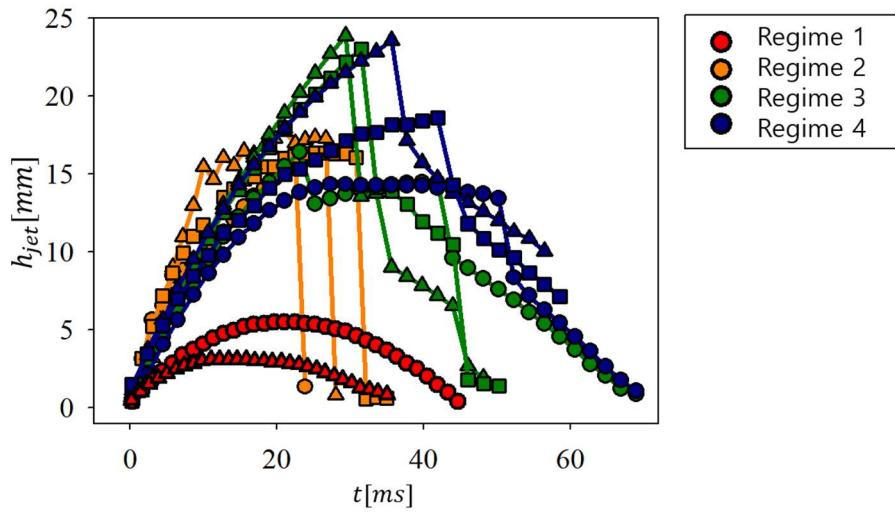


Figure 3.4. Temporal variation of the height of jet for each regime plot on a single graph: Regime 1 (●), Regime 2 (◻), Regime 3 (▲), Regime 4 (●)

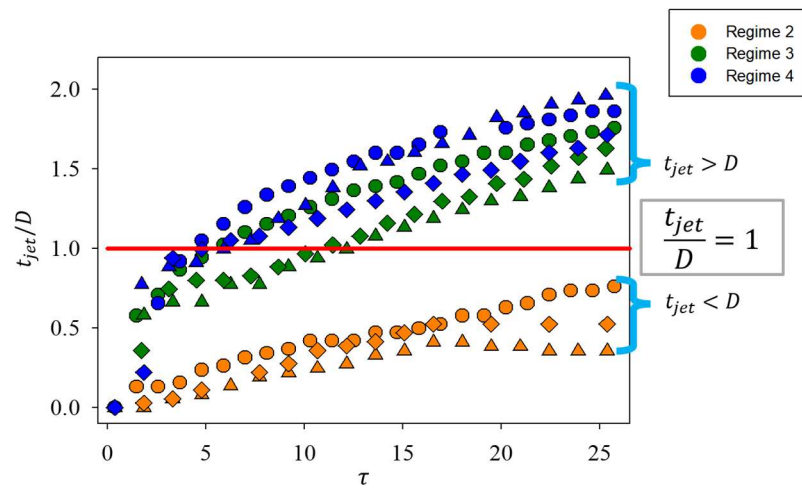


Figure 3.5. Temporal variation of the thickness of jet for each regime: Regime 2 (●), Regime 3 (●), Regime 4 (●)

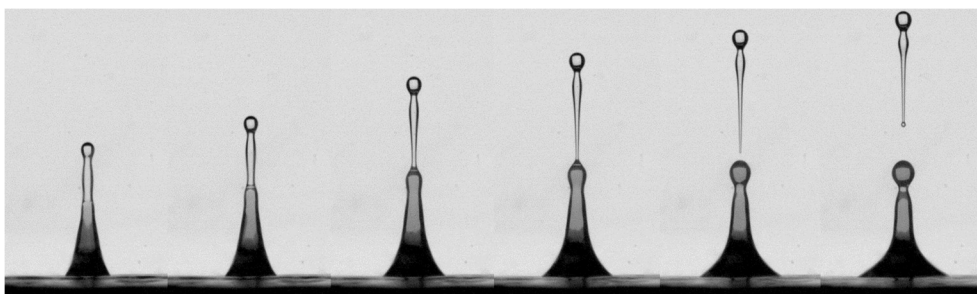
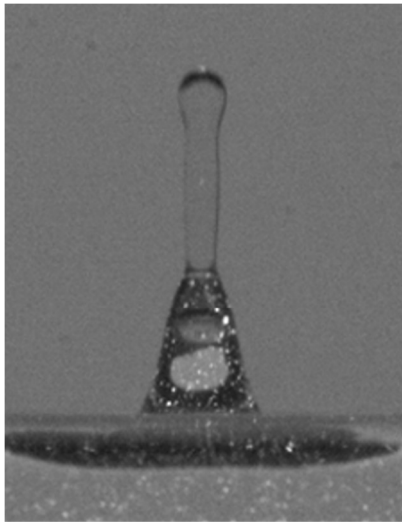
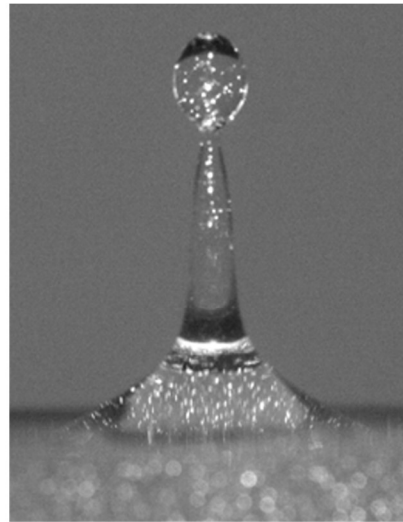


Figure 3.6. The images of the jet when a 20 cSt oil droplet is dropped into the dyed water show that a secondary droplet of oil is formed.



(a)



(b)

Figure 3.7. The images of the jet that appears when (a) 10 cSt oil droplet; (b) 100cSt oil droplet is dropped into water mixed with water-only particles reveal the composition of the secondary droplet.

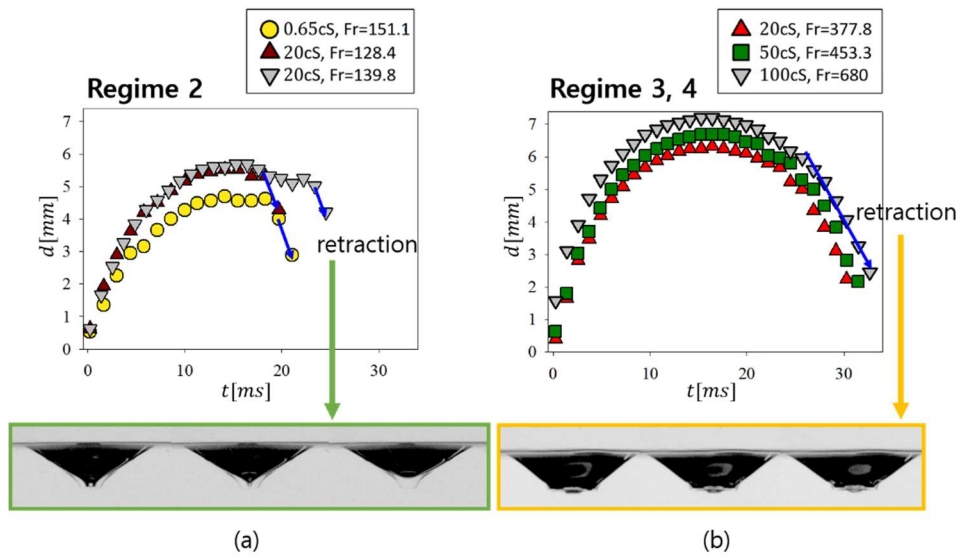


Figure 3.8. crater depth graph corresponding to (a) regime2; (b) regime3, 4.  $t=0$  is the moment of impact, and an image of the moment of retraction is shown below.

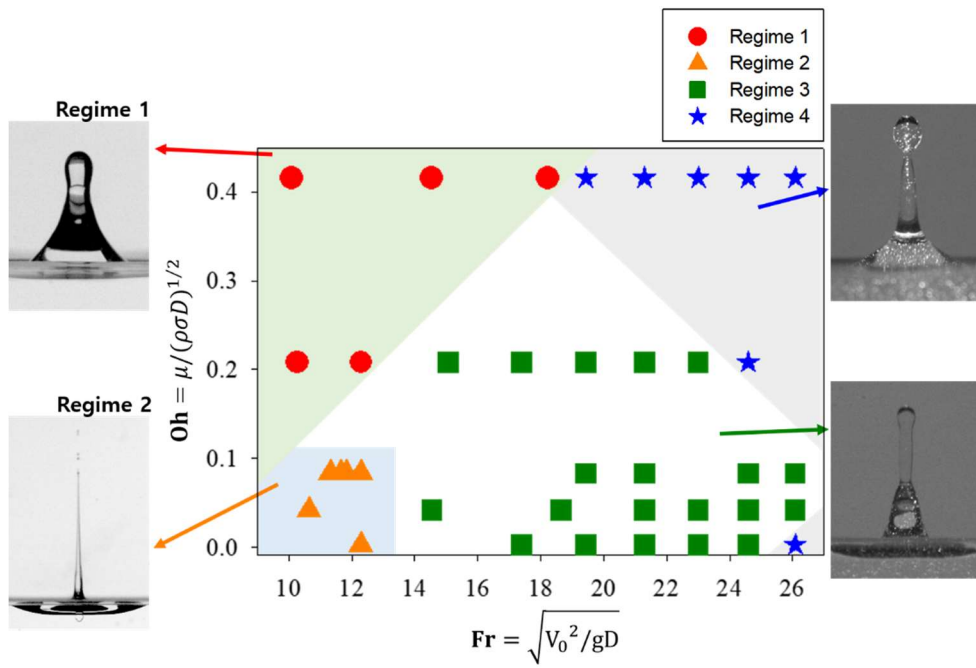


Figure 3.9. Regime map for  $Fr$  and  $Oh$  numbers: Regime 1 (●), Regime 2 (▲), Regime 3 (■), Regime 4 (★)

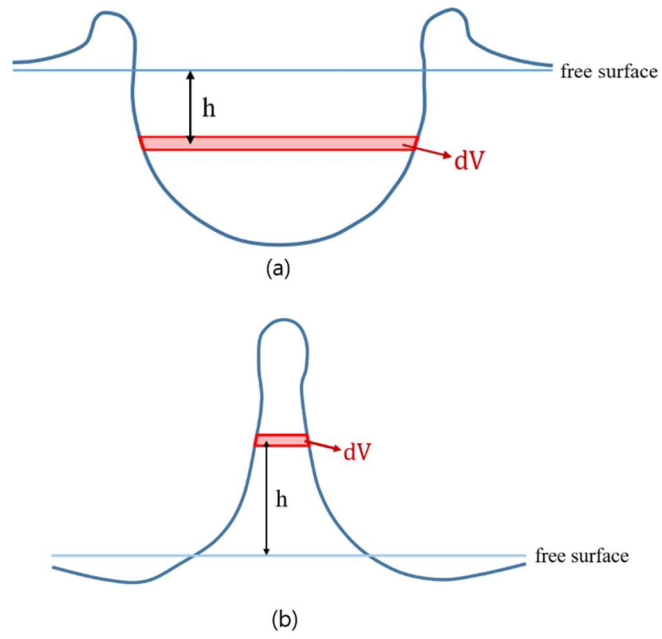


Figure 3.10. Illustration of the  $dV$  of the (a) crater and (b) jet to determine the potential energy.

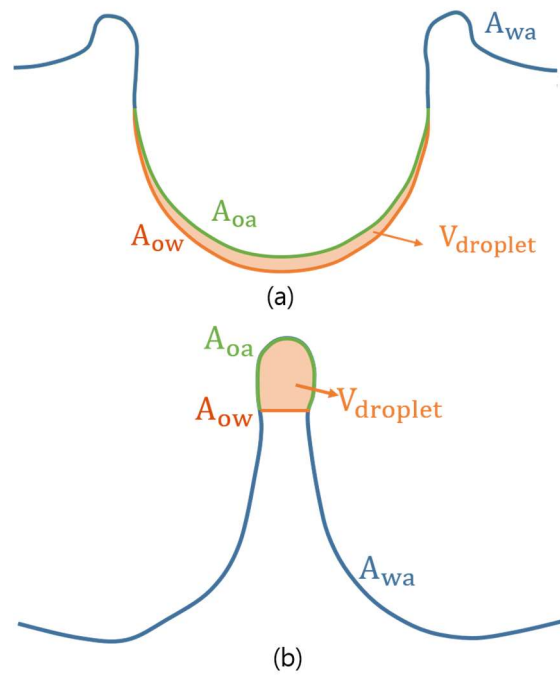
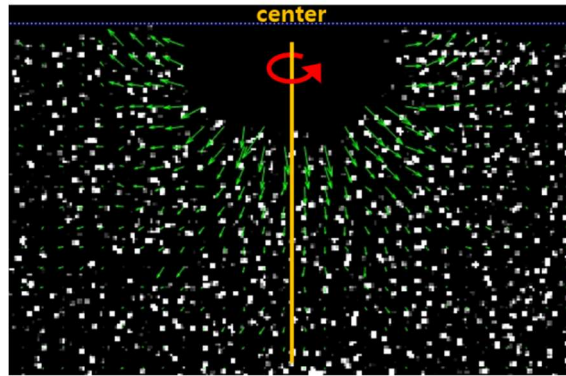
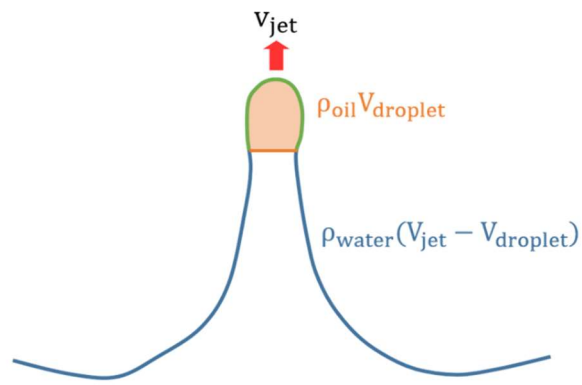


Figure 3.11. Illustration of the  $A_{ow}$ ,  $A_{oa}$ , and  $A_{wa}$  of the (a) crater and (b) jet to determine the surface energy.



(a)



(b)

Figure 3.12. (a) Representation of the PIV results, where the 2-D results are three-dimensionalized through the axisymmetry assumption; (b) Illustration of the  $v_{jet}$  of the jet to determine the kinetic energy.

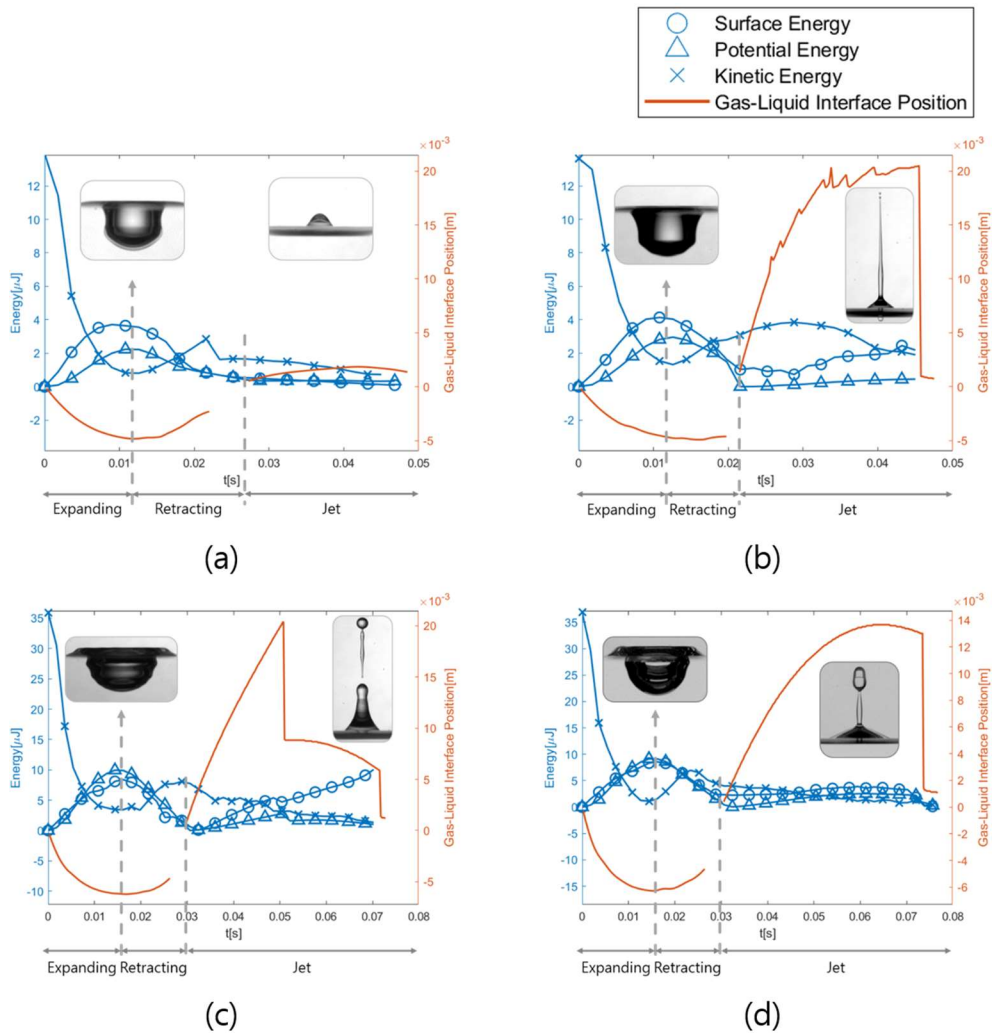


Figure 3.13. Surface energy, potential energy, kinetic energy, and gas–liquid interface position over time for (a) Regime 1, (b) Regime 2, (c) Regime 3, (d) Regime 4: surface energy ( $\circ$ ), potential energy ( $\triangle$ ), kinetic energy ( $\times$ ), gas–liquid interface position (—, orange line)

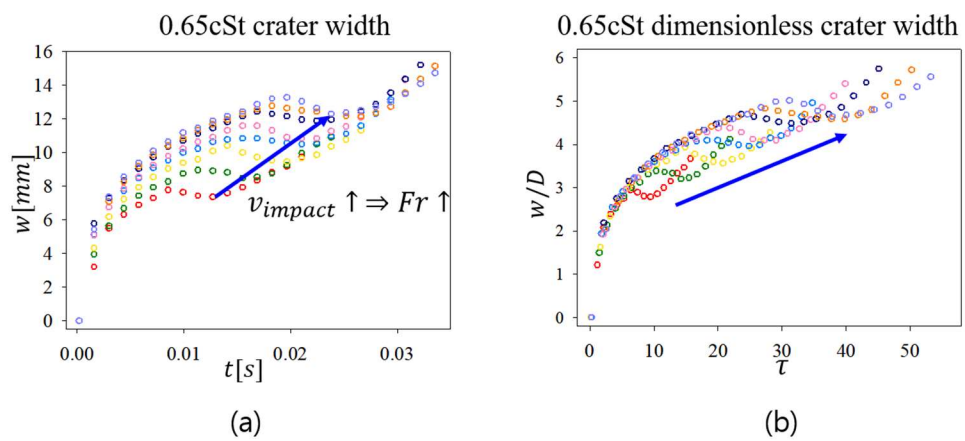


Figure 3.14. (a)  $t-w$  graph when 0.65cSt oil droplet impact, (b)  $\tau-w/D$  graph (Nondimensionalize)

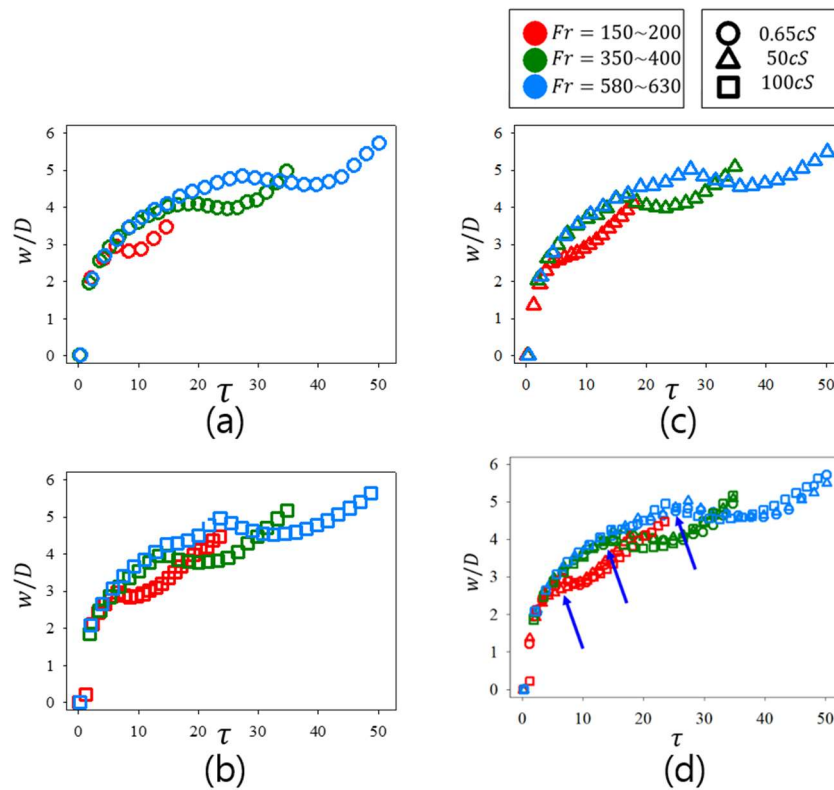


Figure 3.15. Represent three cases for each viscosity,  $Fr=150-200$ ,  $350-400$ , and  $580-630$  (a)  $0.65 \text{ cSt}$ , (b)  $50 \text{ cSt}$ , and (c)  $100 \text{ cSt}$ .

(d) Plotting the nine cases of (a), (b), and (c) on one graph to show that the points of departure from the curve are similar for each range of  $Fr$ .

$0.65 \text{ cSt}(\bigcirc)$ ,  $50 \text{ cSt}(\triangle)$ ,  $100 \text{ cSt}(\square)$ ;  $Fr=150 \sim 200(\bullet)$ ,  $Fr=350 \sim 400(\bullet)$ ,  $Fr=580 \sim 630(\bullet)$

# Chapter 4

## Conclusion

In the present research, we aimed to demonstrate experimentally how the viscosity of an oil droplet influences the dynamics that occur when it collides with the immiscible bulk water. To investigate the crater and jet dynamics caused by dropping an immiscible silicon oil droplet into deep water, we varied the oil droplet's impact velocity and the silicon oil's viscosity. To analyze the behavior of the crater and jet following the impact of a drop, we used a high-speed camera with a light source behind the tank to acquire shadowgraphy images of the crater and jet. In addition, we utilized high-speed two-phase particle image velocimetry to calculate the kinetic energy and observe the temporal velocity field of the fluid beneath the water's surface following the impact. We were able to observe the composition of the secondary droplets using the same apparatus.

When the crater width graphs were plotted against dimensionless time as a function of impact velocity and drop diameter, they all resembled an s-shaped curve that separated from the main curve at some point. The dimensionless time  $\tau$  at that moment was determined by the oil droplet's impact velocity. As a consequence, we discovered that the crater width is a parameter that is independent of the viscosity of the droplet and only depends on the impact velocity. In addition, we classified the jet's behavior according to pinch-off, jet thickness, and secondary droplet composition: R1. jet with no pinch-offs; R2. thin and rapid jet with

upper pinch-offs; R3. secondary oil droplets at upper pinch-offs; R4. secondary oil and water droplets at upper pinch-offs.

The graph of jet height over time for each regime is continuous in regime 1 because there is no pinch-off, but discontinuous in regimes 2, 3, and 4 due to the dives section caused by pinch-off. The pinch-off with small secondary droplets, the pinch-off with large secondary droplets, and the number of pinch-offs varied depending on the pinch-off characteristics of each regime. Regime 2 describes the situation in which the jet is narrower than the initial droplet. By dyeing the water in the tank and using particles and lasers to visualize it, we were able to determine the composition of the secondary droplets generated by the pinch-off of the jet, which corresponds to regime 3 when droplets consisting primarily of oil are generated and regime 4 when droplets consisting of a mixture of oil and water are generated.

As a function of time, we determined the gravitational potential energy, surface energy, and kinetic energy. This allowed us to compare the very low jet of regime 1 with the rapid, thin, and high jet of regime 2, which were vastly different despite having the same initial droplet energy. In the case of high viscosity, viscous dissipation is significant, resulting in a low conversion of crater energy to jet energy and a low and sluggish jet, whereas in the case of low viscosity, viscous dissipation is minimal, resulting in an adequate transfer of jet energy and a high and fast jet.

While we have conducted experiments with Fr numbers ranging from 100 to 630 and Oh numbers ranging from 0 to 0.42 in this investigation. To determine whether regime 1 occurs when the Fr number is smaller at low viscosity and regime 4 occurs when the Fr

number is larger, it is necessary to conduct additional experiments with  $Fr$  and  $Oh$  numbers other than those used in this study. Additionally, it is essential to investigate whether the energy conversion by viscous dissipation is less when a droplet of oil with a higher viscosity falls down. Although we have confirmed that viscous dissipation converts less energy at higher viscosities, this must be clarified through mathematical modeling of viscous dissipation. In addition, the surface tension of silicon oil in this study is approximately 20 mN/m, which differs from the surface tension of water, which is 72.5 mN/m; therefore, it is necessary to investigate the effect of this and the density difference. In addition, it will be possible to determine the drop impact dynamics for a variety of parameters by examining the impact dynamics of liquid pools other than water, which have not been adequately investigated to date.

## Bibliography

- Bussmann M., Chandra S., Mostaghimi J., "Modeling the splash of a droplet impacting a solid surface," *Phys. Fluids* **12**, 3121–3132 (2000)
- Caviezel D., Narayanan C., Lakehal D., "Adherence and Bouncing of Liquid Droplets Impacting on Dry Surfaces," *Microfluidics and Nanofluidics* **5**, 469–78 (2008).
- Chaudhuri J., Mandal T. K., Bandyopadhyay D., "Influence of the pre-impact shape of an oil droplet on the post-impact flow dynamics at air–water interface," *Soft Matter*. **18**, 4102 (2017).
- Chen N., Chen H., Amirfazli A., "Drop impact onto a thin film: Miscibility effect," *Physics of Fluids* **29**, 092106 (2017)
- Cossali G. E. , Coghe A., Marengo M., "The impact of a single drop on a wetted solid surface.," *Exp. Fluids* **22**, 463–472 (1997)
- Das S. K., Dalal A., Breuer M., Biswas G., "Evolution of Jets During Drop Impact on a Deep Liquid Pool," *Physics of Fluids* **34**, (2022).
- Deka H., Ray B., Biswas G., Dalal A., Tsai P.–H., Wang A.–B., "The Regime of Large Bubble Entrapment During a Single Drop Impact on a Liquid Pool," *Physics of Fluids* **29**, (2017).
- Dhuper K., Guleria S. D., Kumar P., "Interface Dynamics at the Impact of a Drop onto a Deep Pool of Immiscible Liquid," *Chemical Engineering Science* **237**, 116541 (2021).
- Goebel A. and Lunkenheimer K., "Interfacial tension of the water/n–

- alkane interface." *Langmuir* **13.2**: 369–372. (1997)
- Kim H. and Park H., "Bubble Dynamics and Induced Flow in a Subcooled Nucleate Pool Boiling with Varying Subcooled Temperature," *International Journal of Heat and Mass Transfer* **183**, 122054 (2022).
- Lee, J., & Park, H., "Wake structures behind an oscillating bubble rising close to a vertical wall," *Int. J. Multiphase Flow*, **91**, 225–242(2017).
- Lee J. S., Weon B. M., Park S. J., Kim J. T., Pyo J., Fezzaa K., Je J. H., "Air Evolution During Drop Impact on Liquid Pool," *Scientific reports* **10**, 5790 (2020).
- Lhuissier H., Sun C., Prosperetti A., Lohse D., "Drop Fragmentation at Impact onto a Bath of an Immiscible Liquid," *Physical review letters* **110**, 264503 (2013).
- Ma H., Liu C., Li X., Huang H., Dong J., "Deformation Characteristics and Energy Conversion During Droplet Impact on a Water Surface," *Physics of Fluids* **31**, (2019).
- Maeng H. and Park H., "Variation of wall heat transfer on a vertical heated wall due to a single rising bubble," *material thesis of Seoul National University* (2020).
- Maeng H. and Park H., "An Experimental Study on the Heat Transfer by a Single Bubble Wake Rising near a Vertical Heated Wall," *International Journal of Heat and Mass Transfer* **165**, 120590 (2021).
- Michon, G. J., Josserand C., S'eon T., "Jet dynamics post drop

impact on a deep pool,” *Physical Review Fluid* **2**, 023601 (2017).

Yakhshi-Tahti E., Cho H. J., Kumar R., “Impact of drops on the surface of immiscible liquids,” *Journal of Colloid and Interface Science* **350**, 373–376 (2010).

Yarin A. L., “Drop Impact Dynamics: Splashing, Spreading, Receding, Bouncing...,” *Annu. Rev. Fluid Mech.* **38**, 159–192 (2006).

# 국문 초록

액체, 고체 등 다양한 표면에 대한 액적 충돌 역학에 대한 연구는 활발히 이루어지고 있지만, 비혼화성 액체에 대한 연구에서 액적의 다양한 특성이 현상에 끼치는 영향에 대해서는 부족하다. 이 연구에서는 다양한 점도의 실리콘 오일 액적이 깊이가 있는 물에 다양한 충격 속도로 충돌하는 실험을 수행했다. 이 실험은 물 표면 아래로 형성된 크레이터와 위에 나타나는 제트의 역학에 대한 액적의 점도와 프루드 수의 영향을 조사하는 것이다. 고속 새도그래피를 활용하여 크레이터의 크기 등과 제트의 여러 파라미터를 측정할 수 있었다. 제트의 거동 분석을 통해 후속 현상을 네 가지 영역으로 분류하였고, 점도 변화와 프루드 수 측면에서 근본적인 메커니즘을 설명했습니다. 영역을 분류하는 기준은 핀치 오프가 일어나는지, 제트 두께가 초기 액적 직경보다 작은지, 2차 액적의 오일로만 이루어졌는지, 물과 혼합되어 있는지 여부이다. 특히 2차 액적의 성분을 확인하기 위해서 염색한 물, 또는 파티클을 섞은 물에 액적을 충돌시키는 두 가지 시각화 방법을 사용했다. 무차원 크레이터 폭을 무차원 시간에 대해 나타낸 결과, 모든 실험 사례에서 동일한 주곡선을 따라가다가 분리되는 S자형 곡선을 보였으며, 분리 지점은  $Fr$  수치에 의해 결정되는 것을 확인했다. 또한 초고속카메라를 통한 이상-입자유동영상계를 통해 크레이터 주변의 속도장을 측정하고 운동, 위치 및 표면 에너지 측면에서 에너지 분석을 수행하여 각 영역에서 설명된 메커니즘을 설명하고자 하였다. 고점도의 액적의 경우 점성소산으로 인하여 크레이터에서 젯으로 변할 때, 에너지 전달이 저점도에 비해 적었고, 이로 인하여 초기 액적 에너지가 같음에도 불구하고 고점도에서는 속도가 매우 느리며 높이가 매우 낮은 제트가 발생하고, 저점도에서는 매우 빠른 속도로 매우 높은 높이에 도달하며 수많은 핀치오프를 동반하는 제트가 발생하는 차이를 보였다.

핵심어 : 액적, 점도, 크레이터, 제트, 펀치오프, 2차 액적, 에너지 전달, 점성 소산

학번 : 2021-20098